Signal, Image and Video Processing
https://doi.org/10.1007/s11760-024-03092-6

ORIGINAL PAPER

Image enhancement and blur pixel identification with optimization-enabled deep learning for image restoration

S. P. Premnath[1] · P. Sheela Gowr[2] · J. P. Ananth[3] · Sajeev Ram Arumugam[3,4]

Received: 5 June 2023 / Revised: 30 September 2023 / Accepted: 16 February 2024

Abstract
Image enhancement is the process of enhancing specific aspects of an image, such as its borders or contrast. The procedure of restoring a destroyed image is known as image restoration. A multitude of factors, such as low camera resolution, motion blur, noise, and others, can cause images to degrade throughout the acquisition process. Although image restoration techniques can remove haze from a degraded image, they are problematic for use in a real-time system since they necessitate numerous photographs from the same location. The suggested fractional Jaya Bat algorithm (FJBA) provides picture enhancement and blur pixel identification to address this issue. Firstly, the blur pixel identification is done using a deep residual network (DRN) trained with FJBA considering blurry image. FJBA is created by combining the Jaya Bat algorithm (JBA) and fractional notion (FC). Furthermore, a blurred image is deblurred using a fusion convolutional neural network (CNN) approach tuned through Pelican hunter optimization (PHO). PHO stands for Pelican optimization (PO) and hunter prey optimization (HPO). Lastly, the image is enhanced using the neural fuzzy system (NFS) and the image enhancement conditional generative adversarial network (IE-CGAN), which has been fine-tuned using FJBA. The proposed FJBA-NFS-IE-CGAN provided enhanced performance with the highest PSNR of 50.536 dB, SDME of 60.724 dB, and SSIM of 0.963, respectively.

Keywords Blur pixel identification · Deep learning · Image restoration · Neuro-fuzzy system · Image enhancement

1 Introduction

Different kinds of image degradations, such as defocus blur, turbulence in the atmosphere, and motion blur affect the imaging systems. Each of these drastically lowers the visual quality. To improve the performance of imaging systems, it is crucial to create techniques for regaining roughly concealed images from blurry ones. Such techniques will have a wide range of applications in numerous fields. Yet, the subject of blur reduction is a notoriously vague inverse problem that has baffled academics for decades [1]. Blurred images can be analyzed using a point spread function (PSF). The PSF explains how a point source or object spreads throughout an image and mimics how the imaging equipment catches the point source or object. The motion length, defocus radius, and turbulence degree are typically the factors that can be used to turn the PSF into a parametric model [2]. The stationary PSF model is unsuitable in the majority of realistic cases because of the prolonged depth of field [3], anisotropic optical lens aberrations from moving objects or cameras [4], and atmospheric turbulence. A so-called spatially variable blur results from these kinds of image degradation. Recovery of a PSF map that describes the blur kernel at each place of the spatial plane is then required for PSF identification [5, 6]. Image degradations of different degrees are frequently created as part of the acquisition process due to the physical limits of cameras or because of complex lighting circumstances. For instance, smartphone cameras have tiny sensors, a limited aperture, and a constrained dynamic range. They frequently produce noisy and low-contrast images as a result [7].

✉ S. P. Premnath
spremnath959@gmail.com

1 Electronics and Communication Engineering, Sri Krishna College of Engineering and Technology, Coimbatore, Tamilnadu 641008, India

2 Computer Science and Engineering, Vels Institute of Science, Technology and Advanced Studies, Chennai, Tamilnadu 600117, India

3 Computer Science and Engineering, Sri Krishna College of Engineering and Technology, Coimbatore, Tamilnadu 641008, India

4 Department of Artificial Intelligence and Data Science, Sri Krishna College of Engineering and Technology, Coimbatore, Tamilnadu 641008, India

Published online: 12 May 2024

The main objective of image enhancement is to deliver better input for automatic image processing as well as better data comprehension for human users [8]. It has been noted that image enhancement is a challenging technique to enhance the visual appeal of the image or provide enhanced transform modeling for the next automatic image processing. Many methods for improving images have been developed, some of which are based on the improvement of the gray-level histogram, while others are based on edge evaluation, local contrast transformation, or global entropy transformation. This is because strategies for picture enhancement are designed using standards for image quality [9]. The process of enhancing a picture consists of techniques that aid in changing the image for evaluation while enhancing aesthetic appeal. The intention is to make parameters better so that they are appropriate for a given task [10].

Due to the recent rapid progress of deep learning algorithms, numerous computer vision applications for connected autonomous vehicles (CAVs) and advanced driver assistance systems (ADASs) have been developed. These applications primarily concentrate on surveillance systems, semantic segmentation, object detection, object categorization, and object identification [11]. However, they can only be used during the day and in clear weather because the majority of computer vision programs in use today are based on visible light cameras. As a result, even the most advanced models cannot be used to analyze images taken at night [12]. At night, it is challenging to separate target objects from the backdrop because of the ease with which the contour and appearance features of traffic participants get distorted. In light of this, restoring details of low-light photographs is a difficult undertaking, particularly for rural low-light images. Deep learning-based algorithms have demonstrated outstanding success in picture enhancement applications more recently, driven by big datasets and the increase in calculation skills [13]. All of these methods, nevertheless, were limited to using external light sources in low-light conditions. Since those accidents are more likely to occur when driving at night in rural regions without street lighting, an image improvement model that can handle darker conditions is necessary [14].

The aim is to develop an approach for identifying blurry pixels and image enhancement. The process used for identifying blurry pixels and enhancing the image is illustrated. The input image is initially subjected to the identification of a blurred pixel map which is discovered with DRN. The DRN is trained based on FJBA, which is a combination of FC and JBA. Moreover, the images are deblurring using fusion CNN which is tuned by PHO. Additionally, PHO is newly devised through the integration of PO and HPO. After blur pixel map determination, the blurry pixel enhancement is carried out with the statistical technique. Then, the enhancement of the image is performed with a neuro-fuzzy model and IE-CGAN, which is trained with the proposed FJBA.

The key contribution of the paper is given below.

- *Established FJBA_NFS-IE-CGAN for image restoration*: The proposed FJBA-based IE-CGAN and NFS are used to generate the enhanced image. To create the restored image, several upgraded images are joined. In this instance, the IE-CGAN training is carried out using a designed FJBA, which was created by fusing FC and JBA.

Below are the remaining sections: The traditional methods of image restoration and their merits and demerits are described in Sect. 2. An image restoration model is illustrated in Sect. 3. The effectiveness of the developed model is presented in Sect. 4, and the conclusion is developed in Sect. 5.

2 Literature survey

At night, it is challenging to identify target objects from the background because of to ease with which the contour and appearance features of traffic participants blend. As a result, recovering the details of low-light photographs is a challenging task, especially for rural low-light images.

Here the eight conventional approaches for restoring images are discussed along with their benefits and drawbacks. Zhang et al. [15] developed an efficient method named residual dense network (RDN) for image restoration. In this case, the residual dense block (RDB) served as the fundamental building block for RDN, which benefited from the merging of local and global features to gain very potent representational capabilities. RDN provided a favorable trade-off between model size and performance by utilizing fewer network parameters than residual network while outperforming dense network. Based on the scant input data, RDN was unable to recover comparable textures. Chang et al. [16] created the long-short-exposure fusion network (LSFNet) to address the issues with low-light picture fusion, such as high noise, motion blur, color distortion, and misalignment. Here, the technique used the complimentary data from photos taken under short and long exposures. Since the acquired photographs were of poor quality, the supplementary data was not taken into account. Yang et al. [2] devised a method named general regression neural network (GRNN) for blur image recognition. Even though there were a lot of inputs, the GRNN's advantages in this situation were quick learning and convergence. However, the primary drawback of the GRNN was its enormous size, which necessitated costly calculations. Huang and Xia [17] introduced a joint blur kernel estimation and CNN method for blind image restoration. In this case, the hybrid blur kernel estimation and CNN approach outperformed traditional blind picture restoration techniques in terms of restoration quality and processing

speed. Nevertheless, this method's cost function was non-convex.

Huang et al. [6] devised a 1D state-space model to describe the statistical dependence among the neighboring kernels. Here, this method unlocked a wide range of opportunities outside of the work. As an illustration, various noise distributions were utilized right away. Markovian state-space models and other alternatives were not taken into account. Wang [18] established a new wavelet transform-based image restoration technique for national parks. Using the similarities and differences of the original image as a starting point, the wavelet transform-based image enhancement technique used in this case, which was based on the wavelet transform approach, evaluated and fused many images to restore the original image. This method was unable to enhance the overall enhancing effect. Zamir et al. [7] introduced MIRNet-v2 for fast image restoration and enhancement. Less time was required for training using this strategy. However, this method did not take into account more useful elements for improving image restoration. Panetta et al. [19] introduced a deep perceptual image enhancement network (DPIENet) for exposure restoration. Here, DPIENet was used to get rid of artifacts that can arise with a few existing techniques, like halo effects, noise amplification in dark areas, and artificial color production. Super-resolution, image recoloring, and denoising were only a few of the low-level computer vision tasks for which the system's accuracy was regrettably not examined.

3 Proposed fractional Jaya Bat algorithm_neural fuzzy system image enhancement conditional generative adversarial network (FJBA_NFS-IE-CGAN) for image restoration

An image's edges or contrast are sharpened during the process of image enhancement to produce a graphic display that is suitable for study and display. It is applied to enhance visual quality. Moreover, it helps to enhance low-level vision applications. Image restoration is the process of restoring damaged images. Motion blur, poor resolution, and noise are a few examples of corruption's emergence. The limited resolution of the camera, motion blur, noise, and other factors can occasionally cause photos to be degraded throughout the acquisition process. Even though image restoration techniques can successfully remove the haze from a degraded image, they require a large number of photographs from the same area, making it hard to employ them in a real-time system. To bridge this gap, an image enhancement and blur pixel identification enabled by the proposed FJBA is introduced. Initially, the input blurry image which is specified in the dataset [20] is fed up to the blurred pixel identification. After that, the blur pixel identification is done utilizing DRN, which is trained using FJBA. Here, FJBA is obtained by the combination of JBA [21] and FC [22]. Moreover, the blurred image is subjected to the deblurring phase by the fusion CNN method, which is tuned employing PHO. Here, PHO is the integration of PO [23] and HPO [24]. Finally, the image enhancement is accomplished by NFS [25] and IE-CGAN [26], which is finely tuned using FJBA. Figure 1 demonstrates a block diagram of the proposed FJBA_NFS-IE-CGAN for image restoration.

3.1 Image acquisition

Consider image-enhanced input images obtained from a dataset. Assume a database R that contains b photographs and is represented as

$$R = \{\eta_1, \eta_2, \ldots, \eta_m, \ldots, \eta_b\} \tag{1}$$

Here, the total number of images is represented as b, the database is denoted as R, and η_m illustrates mth image. Several image components are corrupted, and the pixels that remain are labeled as blur-free. Due to the complexity of the newly discovered noisy pixels, the DRN was created to assist in finding them by modifying the image's surrounding area.

3.2 Blur pixel identification

To recognize the blurred pixel map, the DRN is modified. The prediction map for image pixels is produced using the DRN [27]. Here, DRN creates a prediction map based on the input image. With increased precision, DRN is employed to assess visual imagery. It has its challenges and helps in finishing difficult computer vision jobs. It also helps to resolve to explode and vanish gradients when there are several layers added. Here, the DRN is trained by the FJBA algorithm.

To identify the noisy pixel map, the image η_m is used as an input to DRN. A decision on the blurry pixel map finding is made using the DRN [27], which has been modified to produce effective decisions.

The input image taken into consideration, in this case, has a center normalization of zero and it is $32 \times 32 \times 3$ size. In this case, the output is indicated as η_S, which helps in identifying noisy pixel maps.

3.2.1 Training of DRN with FJBA for image restoration

The FJBA algorithm, which was created for blur pixel recognition, is briefly explained in this section. The developed FJBA is newly devised by the integration of the fractional

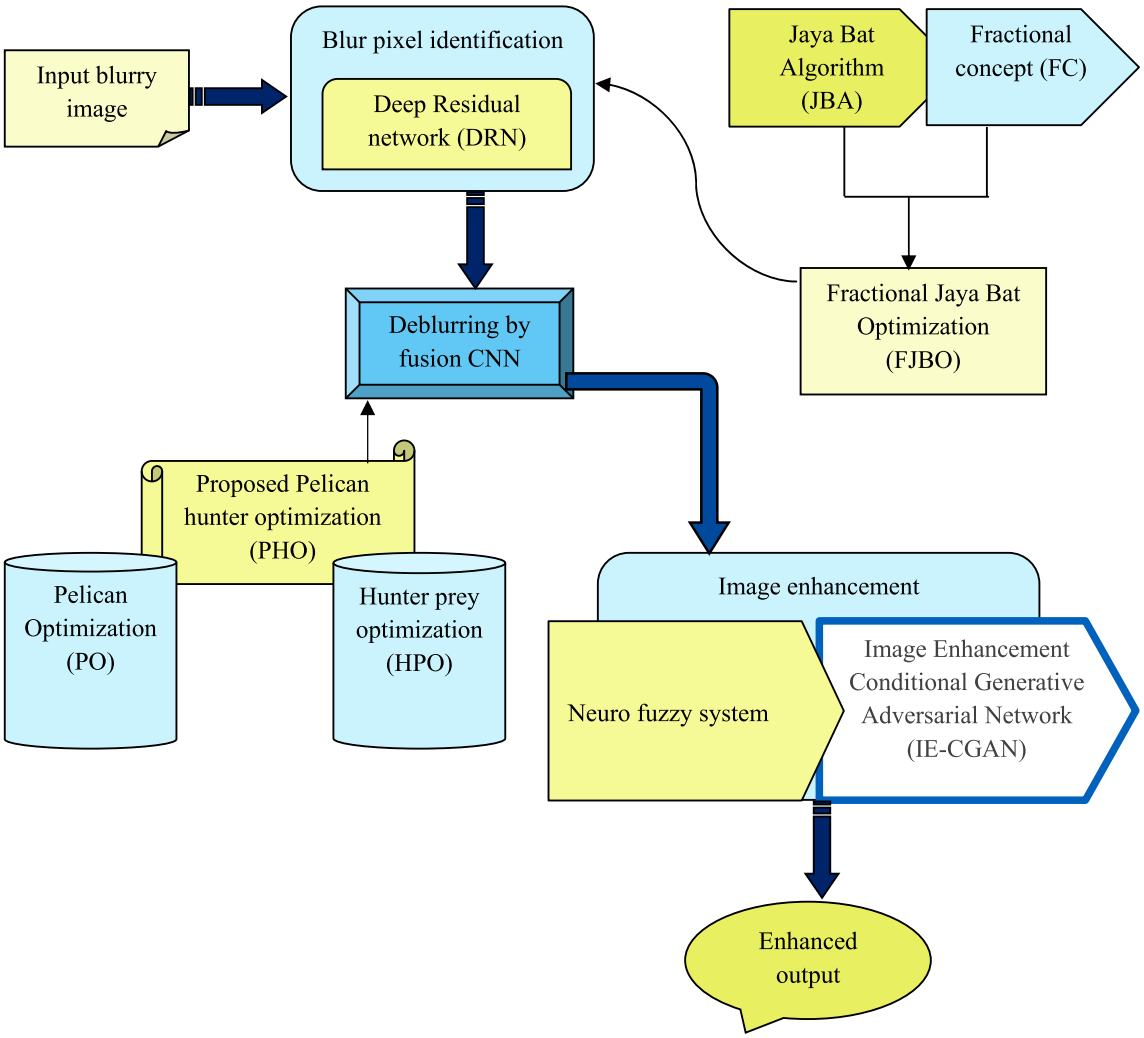

Fig. 1 Block diagram of FJBA_NFS- IE-CGAN for image restoration

concept [28] and JBO [21]. Moreover, JBO is the combination of the Jaya optimization algorithm (JOA) [29] and the bat algorithm (BA) [30]. Creating a hybrid Jaya Bat algorithm [21] is driven by the desire to combine the finest aspects of both algorithms. The basic concept is to update the Jaya particle's location, adjust frequencies, update bats' velocities and positions, and acquire the current best and worst solutions for both algorithms. The BA [30] is inspired by the microbats' echolocation traits. This technique is particularly effective in producing enhanced features to address multi-objective optimization issues. Furthermore, it can resolve difficult constrained highly nonlinear problems. Jaya [29] is carried out using candidate solutions, and this structure operates regardless of any parameters. Due to its singular phase of operation, the Jaya algorithm is easier to use. The features are combined using a fractional idea, which is then used to organize the features using fractional calculus [28]. The FC is used to assess the best solution based on the previous iterations and is designed to acquire the sequential features. The improvement makes the solution update more effective and raises the effectiveness of the suggested optimization procedure. The following sections provide descriptions of each of the several algorithmic steps that comprise the DRN training procedure.

Step (i): Initialization

Initialization is the primary stage, which is signified by F with l number of solutions.

$$F = \left\{D_1, D_2, \ldots, D_j, \ldots, D_l\right\} \tag{2}$$

wherein D_j refers to jth solution, l represents a total solution in the database, and F indicates database.

Step (ii): Evaluating fitness function

The fitness function employs the error function to determine the best course of action, as seen in Eq. (3) below.

$$\mathrm{MSE}_{\mathrm{fit}} = \frac{1}{P}\sum_{S=1}^{P}\left[\eta_S^* - \eta_S\right]^2 \tag{3}$$

Here, the total number of training samples is indicated as P, η_S is the classified output, and targeted output is signified as η_S^*.

Step (iii): Integration of FC and JBA

The solution is updated with its location using the bat algorithm after the objective function has been computed. The standard equation of the FC algorithm is also incorporated into the standard equation of the JBA algorithm to reduce optimization problems and improve algorithm performance. The JBA update equation is written as to increase overall performance.

$$E_{\wp+1}^{w} = \frac{G_{\wp+1}^{w} J_1 + \left[T_0 + T_1(E_{\wp-1}^{w} + \Upsilon(E_{\wp-1}^{w})) + T_2(E_{\wp-2}^{w} + \Upsilon(E_{\wp-2}^{w}))\right] (\wp_1 - (1+J_2)\cdot n^w) + J_2 E^{\mathrm{worst}} n^w}{\wp_1 - n^w} \tag{4}$$

Applying fractional concept [28], the update Eq. (4) of location is articulated as,

$$U^{\delta}\left[E_{\wp+1}^{w}\right] = \frac{1}{\wp_1 - n^w} \times \left[\frac{G_{\wp+1}^{w} J_1 + \left[T_0 + T_1(E_{\wp-1}^{w} + \Upsilon(E_{\wp-1}^{w})) + T_2(E_{\wp-2}^{w} + \Upsilon(E_{\wp-2}^{w}))\right]}{(\wp_1 - (1+J_2)\cdot n^w) + J_2 E^{\mathrm{worst}} n^w}\right] \tag{5}$$

$$\begin{aligned} E_{\wp+1}^{w} = {} & \frac{1}{\wp_1 - n^w} \times \left[\frac{G_{\wp+1}^{w} J_1 + \left[T_0 + T_1(E_{\wp-1}^{w} + \Upsilon(E_{\wp-1}^{w})) + T_2(E_{\wp-2}^{w} + \Upsilon(E_{\wp-2}^{w}))\right]}{(\wp_1 - (1+J_2)\cdot n^w) + J_2 E^{\mathrm{worst}} n^w}\right] \\ & + \delta U_{\wp}^{w} + \frac{1}{2}\delta U_{\wp-1}^{w} + \frac{1}{6}(1-\delta)E_{\wp-2}^{w} \\ & + \frac{1}{24}\delta(1-\delta)(2-\delta)U_{\wp-3}^{w} \end{aligned} \tag{6}$$

Here, $\Upsilon(E_{\wp-1}^{w})$ signifies fitness value wth variable at $\wp-1$, $\Upsilon(E_{\wp-2}^{w})$ signifies fitness value w^{th} variable at $\wp-2$, unknown parameter vector is represented as T_0, arbitrary numbers ranging numbers (0, 1) random vector between (0, 1) denoted as Υ, and worst candidate solution is denoted as E^{worst}.

Step (iv): Re-evaluating the fitness

After the updating procedure is complete, Eq. (3) is used to determine the fault. For image enhancement, the solution with the minimum fault is utilized.

Step (v): Termination

The aforementioned procedures are repeatedly carried out until the termination condition is satisfied.

3.3 Deblurring by fusion CNN

The image η_S marked as blurry from the blur detection process is deblurred using the fusion CNN classifier [31]. The PHO method is used by the fusion CNN classifier and is highly effective. The advantage of PO is its excellent ability to explore a wide area in the realm of problem-solving and its power to discover the optimal local site. Nine real-world issues are used to evaluate the benefit of HPO. As a result, the PO and HPO algorithms are integrated to offer a good way to address optimization problems.

The output obtained from fusion CNN is λ_d.

3.3.1 Training of fusion CNN

The fusion CNN is tuned using an established PHO algorithm for deblurring the frame. For effective deblurring of the frame, the designed PHO algorithm incorporates the fertility evaluation of PO [23] into the cyclone foraging behavior of HPO [24]. The PHO algorithm-based fused CNN's proposed algorithmic steps are as follows:

Step 1: Initialization

Initially, Eq. (7) is used to set the initial population. The expression is given below:

$$\overrightarrow{\omega} = \left\{\overrightarrow{\omega_1}, \overrightarrow{\omega_2}, \ldots, \overrightarrow{\omega_o}, \ldots, \overrightarrow{\omega_n}\right\} \tag{7}$$

Here, n represents the total number of solutions, ω signifies database, and ω_o indicates oth solution.

Step 2: Evaluating fitness function

The error function is used to find the optimal solution, which is then applied to the minimization problem and represented as,

$$\mathrm{MSE}_{\mathrm{fit}} = \frac{1}{P}\sum_{S=1}^{P}\left[\lambda_d^* - \lambda_d\right]^2 \tag{8}$$

Here, the number of data is denoted as P, the expected result is $\lambda_d{}^*$, and classified output from fusion CNN is λ_d.

Step 3: Hunter search mechanism

Equation (9) is used in HPO to depict the hunter search mechanism.

$$\omega_{k,z}(r+1) = \omega_{k,z}(r) + 0.5[(2AV\ Q_{\text{pos}(z)} - \omega_{k,z}(r)) + (2(1 - AV\ P_{(z)} - \omega_{k,z}(r))] \quad (9)$$

Here, the current position is indicated as $\omega_{k,z}(r)$, the next level of the hunter is referred to as $\omega_{k,z}(r+1)$, P signifies the mean value of the whole position, the balance parameter is expressed as A, V is the adaptive parameter, and the position of prey is denoted as Q_{pos}, which is given in Eq. (10).

$$\overrightarrow{Q_{\text{pos}}} = \overrightarrow{\omega_k}|k \text{ is sorted } C_{\text{euc}}(O_{\text{best}}) \quad (10)$$

Step 4: The prey fled to safety

When being pursued, the prey will promptly flee to a safe location. The current update of the prey's position is shown in Eq. (11).

$$\omega_{k,z}(r+1) = \hbar_{\text{pos}(z)} + AV\cos(2\pi\Re_4) \times \left(\hbar_{\text{pos}(z)} - \omega_{k,z}(r)\right) \quad (11)$$

$$\omega_{k,z}(r+1) = \hbar_{\text{pos}(z)}[1 + AV\cos(2\pi\Re_4)] - AV\cos(2\pi\Re_4)\omega_{k,z}(r) \quad (12)$$

Here, optimal global location is indicated as Q_{pos}, and randomly selected number $[-1, 1]$ is signified as $\Re_4$.

From PO [23], the update equation of position is expressed as,

$$\omega_{k,z}(r+1) = \omega_{k,z}(r) + \text{rand}\,(\Im_F - \Omega \cdot \omega_{k,z}(r)) \quad (13)$$

$$\omega_{k,z}(r) = \frac{\omega_{k,z}(r+1) - \text{rand}\Im_F}{1 - \text{rand}\Omega} \quad (14)$$

Substituting Eq. (14) in Eq. (12), the equation becomes,

$$\omega_{k,z}(r+1) = \hbar_{\text{pos}(z)}[1 + AV\cos(2\pi\Re_4)] - AV\cos(2\pi\Re_4) \times \frac{\omega_{k,z}(r+1) - \text{rand}\Im_F}{1 - \text{rand}\Omega} \quad (15)$$

$$\omega_{k,z}(r+1) = \frac{1}{1 - \text{rand}\Omega + AV\cos(2\pi\Re_4)} \times \begin{bmatrix} (1 - \text{rand}\Omega)\hbar_{\text{pos}(z)}[1 + AV\cos(2\pi\Re_4)] \\ +AV\cos(2\pi\Re_4)\text{rand}\Im_F \end{bmatrix} \quad (16)$$

Equation (16) is used in this situation to update the position of the best solution. Here, a randomly selected number is signified as $rand$, and the optimum global position is indicated as Ω.

Step 5: Re-evaluating the fitness function

After the updating procedure is complete, Eq. (8) is used to determine the fault. For image enhancement, the solution with the minimum fault is utilized.

Step 6: Termination

The aforementioned steps are constantly repeated till the termination condition is satisfied.

3.4 Enhancement of image with neuro-fuzzy-IE-CGAN

The image enhancement is carried out using the proposed FJBO-IE-CGAN and neural fuzzy system once the recovered noisy pixels λ_d are discovered. Image augmentation modifies the image by utilizing various visual effects. The improved image gives an overview of boundaries and edges with excellent dynamic range. The FJBO-IE-CGAN and the neural fuzzy system are briefly explained here.

3.4.1 Neuro-fuzzy system

The neuro-fuzzy model [32] incorporates fuzzy inference systems' explicit knowledge demonstration and ANN's learning capabilities. Here, the noisy pixels λ_d are regarded as an input. The consequence and premise components make up the ANFIS model. The optimization approach is used to tune ANFIS to identify attributes. The nearest neighbor of a noisy pixel is used to produce a novel picture matrix that is supplied as,

$$X_{p1_{\forall B}}(q, v) = \frac{1}{9}\sum_{r=1}^{1}\sum_{n=1}^{1} X_p(q+r, v+n) \quad (17)$$

To solve difficulties with uncertainty, generated new pixel values are passed to the neural fuzzy model.

$$X_{p2_{\forall B}}(q, v) = J_{\text{fuzzy}}(X_p(q, v)) \quad (18)$$

Here, the neuro-fuzzy system is indicated as J_{fuzzy}. Once the neural fuzzy group has been created, the new pixel $X_p(q, v)$ is used as an input to create a new image with a noise pixel-based location.$\aleph$ is the output of the neuro-fuzzy system.

Fig. 2 Architecture of IE-CGAN

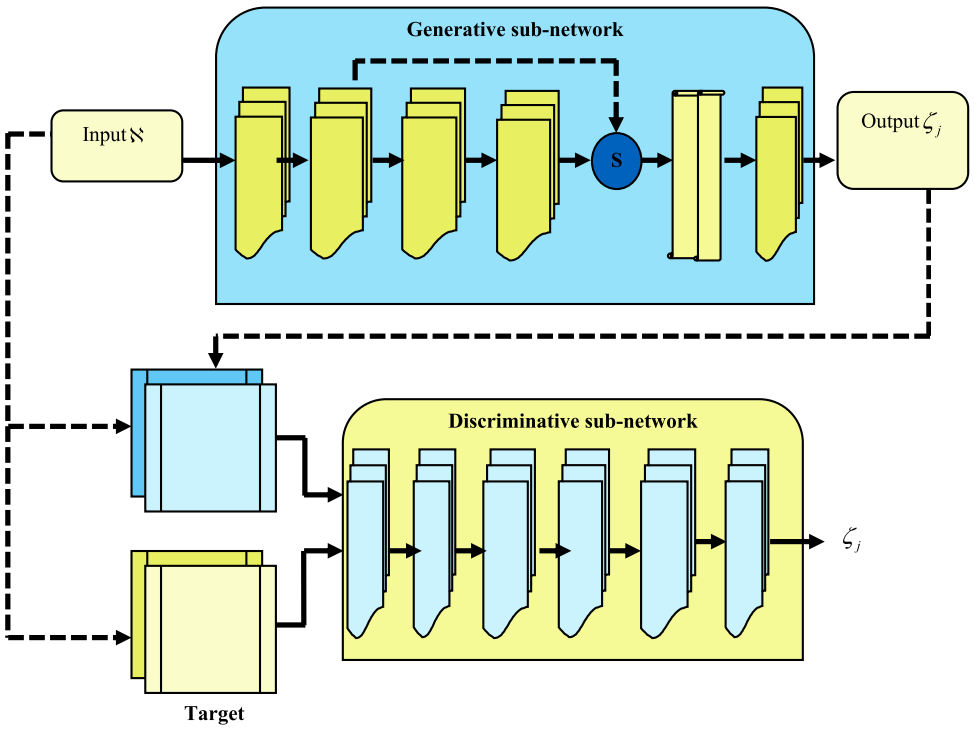

3.4.2 Proposed FJBO-IE-CGAN for image enhancement

Here, the noisy pixels ℵ are taken as input. To train the CGAN, the suggested FJBO is employed. The FC [28] and JBA [21] algorithms are combined to create the suggested FJBO, which was used to adjust the optimum weights. This is a discussion of the CGAN's structure and training utilizing the suggested FJBO.

(i) *Architecture of IE-CGAN*

Generic and discriminative networks are included in the CGAN [33]. The most crucial network was created to enhance contrast, and the most enhanced results are produced when generative networks are supported by discriminative networks. The generative network is trained to trick the discriminative network during training so that it can't tell the difference between improved outputs and its label images.

(a) *Generative sub-network*

For improved results in diverse applications and network performance, image enhancement requires a model. Tanh activation is used to restore concatenated features to their original resolution with a deconvolution layer, and the following generative network is provided.

$$\mathrm{GU} - \mathrm{GSU} - \mathrm{GSU} - \rho - \mathrm{Tanh} \tag{19}$$

Here, the convolutional layer is denoted as G, ReLU is signified as U, batch normalization layer is symbolized as S, deconvolutional layer is represented as ρ, and skip connection is illustrated as t.

(b) *Discriminative sub-network*

The discriminative network's goal is to identify label images that helped the generative sub-network generate promising findings from improved results. The discriminative network is organized as given below,

$$G\Im - GS\Im - GS\Im - GS\Im - G - \varpi \tag{20}$$

Here, the leaky ReLU layer is denoted as $\Im$, and the output attained from IE-CGAN is represented as ζ_j. Figure 2 shows the structural view of IE-CGAN.

3.5 Image enhancement using FJBA

IE-CGAN weights and parameters are optimized utilizing developed FJBA, a hybrid optimization that combines the advantages of both JBA and FC. The FJBA training algorithm is thoroughly studied in Sect. 3.2.1. The fitness parameter used is provided by,

$$\mathrm{MSE}_{\mathrm{fit}} = \frac{1}{P}\sum_{S=1}^{P}\left[\zeta_j^* - \zeta_j\right]^2 \tag{21}$$

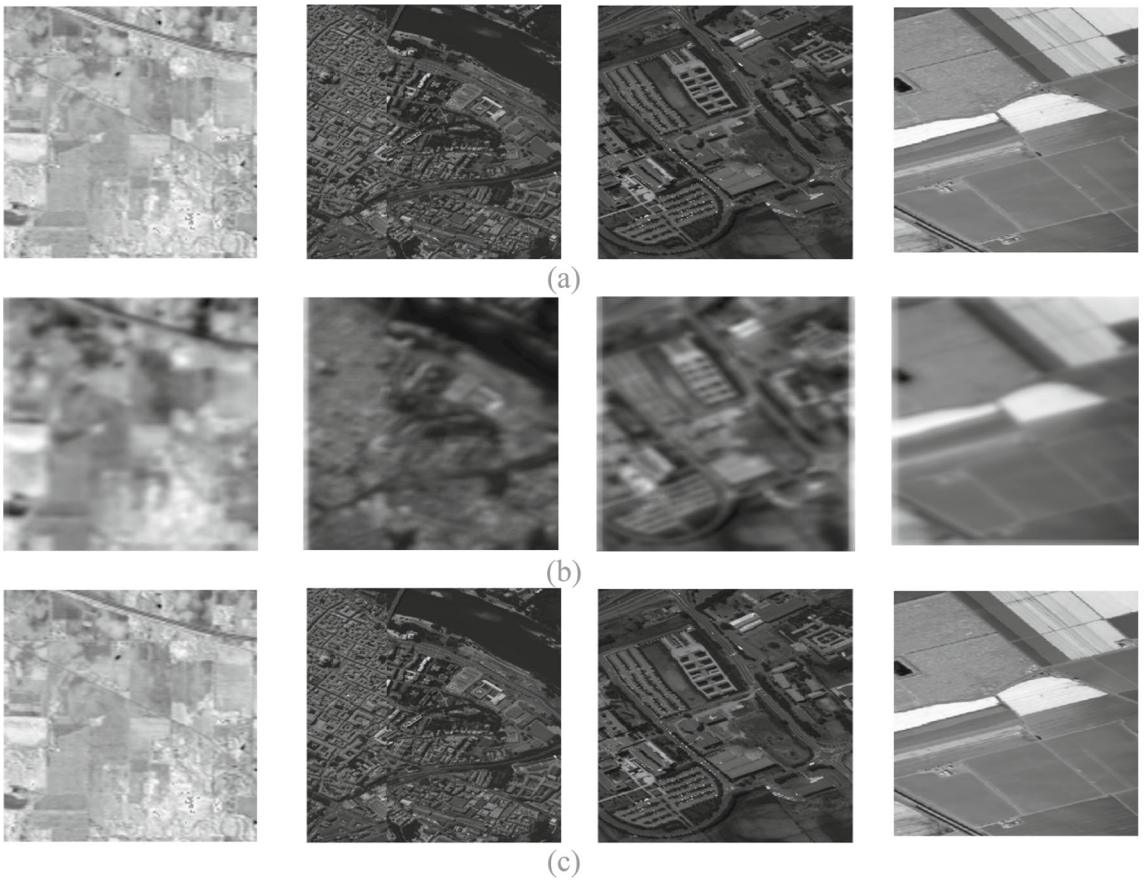

Fig. 3 Experimental findings of the proposed FJBA_NFS-IE-CGAN using Hyperspectral Remote Sensing Scenes dataset with **a** input images of Indian Pines, Pavia Centre and University, Cuprite, and Salinas datasets, **b** blurred images of Indian Pines, Pavia Centre and University, Cuprite, and Salinas datasets, and **c** reconstructed images of Indian Pines, Pavia Centre and University, Cuprite, and Salinas datasets

Fig. 4 Experimental findings of the proposed FJBA_NFS-IE-CGAN using YOLO Object Detection dataset with **a** input image, **b** blurred image, and **c** reconstructed image

Here, the expected output is represented as ζ_j^*, classified output from IE-CGAN is denoted as ζ_j, and the sum of data is indicated as P.

4 Results and discussion

PSNR, SDME, and SSIM are used to calculate the designed FJBA_NFS-IE-CGAN's efficiency. By adjusting the blur intensity, the assessment is conducted.

4.1 Experimental setup and dataset description

With MATLAB, Windows 10 OS, an i3 processor, and 2 GB RAM, the developed model is processed. The dataset used in the evaluation for the proposed method is the Hyperspectral Remote Sensing Scenes and YOLO Object Detection dataset.

Hyperspectral Remote Sensing Scenes This database is collected by M Graña, MA Veganzons, and B Ayerdi. This database has Indian Pines, Salinas, Pavia Centre and University, and Cuprite datasets [20]. It contains information about some hyperspectral scenes that are publicly accessible. These

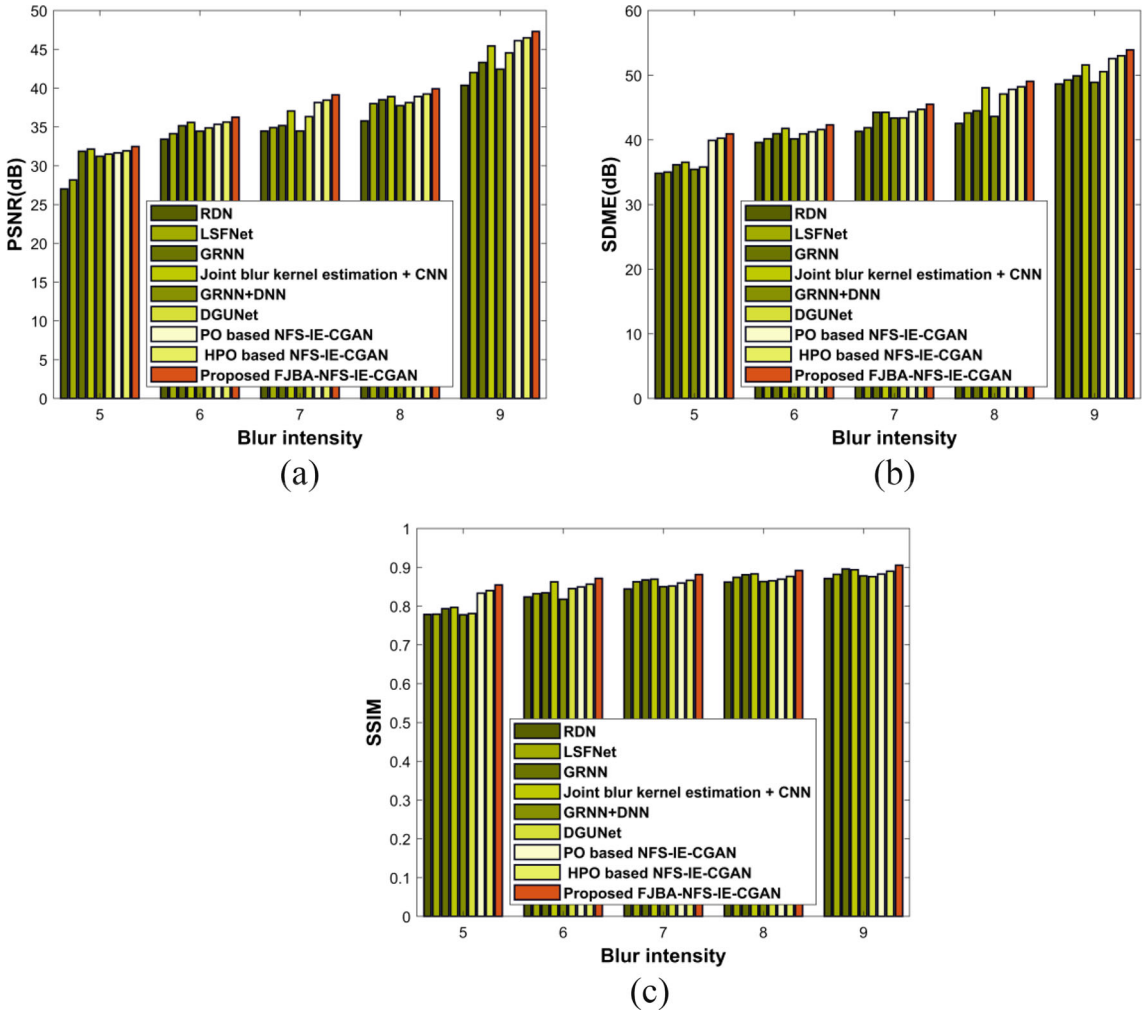

Fig. 5 Assessment with Indian Pines dataset in terms of **a** PSNR, **b** SDME, **c** SSIM

are all Earth Observation images captured by satellites or aircraft.

YOLO Object Detection dataset This dataset contains 80 labels [34], which include bicycles, people, airplanes, cars and trucks, kitchen and dining objects, animals, etc.

4.2 Performance metrics

A few metrics, which are outlined below, are used to assess the effectiveness of the designed FJBA_NFS-IE-CGAN.

(i) *PSNR*

PSNR is used to assess the quality of the outcome and is articulated as,

$$\mathrm{PSNR} = 10\log_{10}\left(255^2 \cdot \iota ||\alpha_{\mathrm{ref}} - \beta_{\mathrm{rest}}||_2^2\right) \tag{22}$$

Here, the reference image is indicated as α_{ref}, the overall number of pixels is denoted as ι, and the restored image is signified as β_{rest}.

(ii) *SDME*

SDME is customized for assessing output image quality and provided by,

$$\mathrm{SDME} = -\frac{1}{\nu_1 \nu_2} \times \sum_{x=1}^{\nu_1}\sum_{y=1}^{\nu_2} 20\ln\left|\frac{L_{\max;\,y,x} - 2L_{\mathrm{center};\,y,x} + 2L_{\min;\,y,x}}{L_{\max;\,y,x} + 2L_{\mathrm{center};\,y,x} + 2L_{\min;\,y,x}}\right| \tag{23}$$

Here, the maximum gray level is denoted as $L_{\max;\,y,x}$, the pixel center is represented as $J_{\mathrm{center};\,y,x}$, and the minimal degree of gray is signified as $L_{\min;\,y,x}$.

(iii) *SSIM*

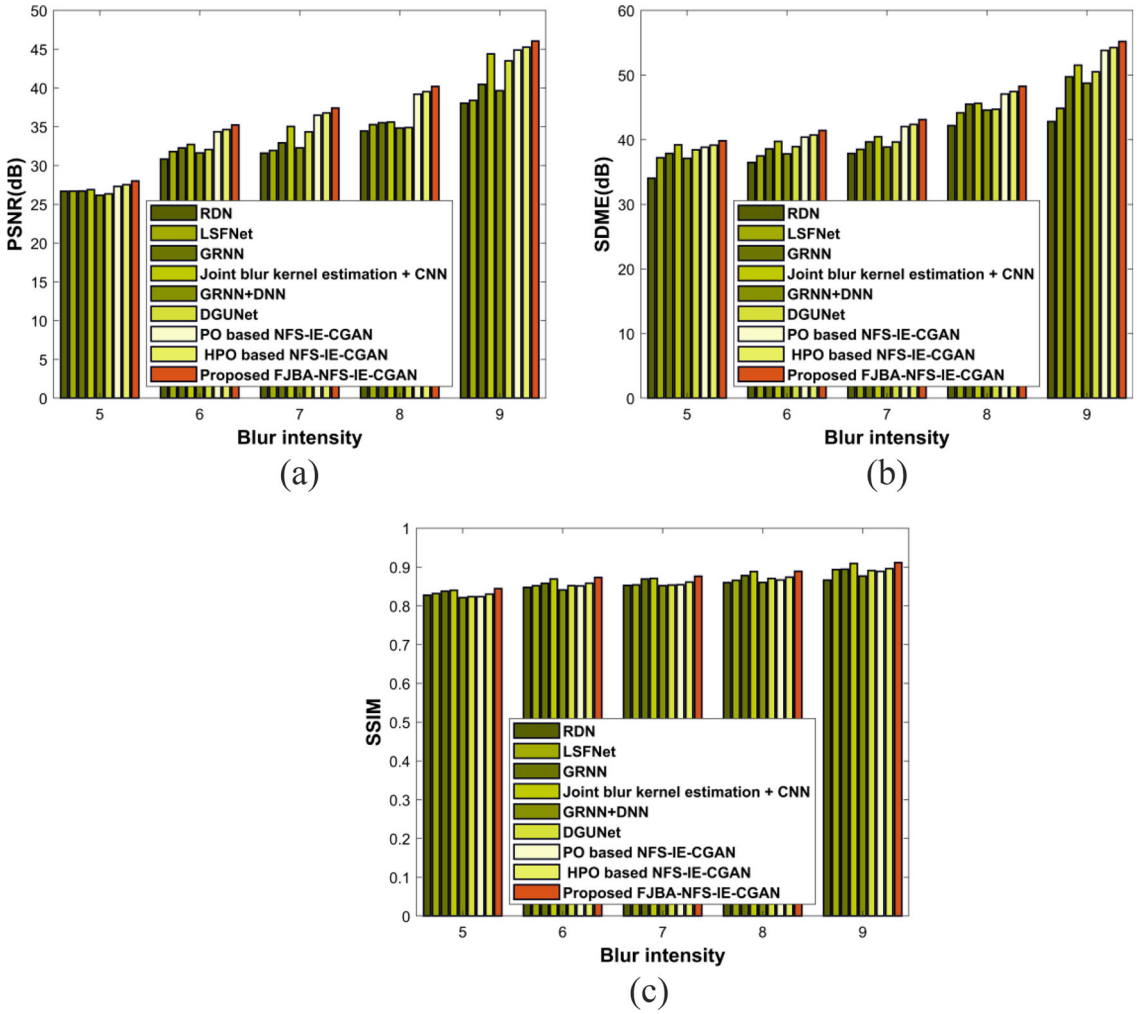

Fig. 6 Evaluation with Salinas dataset based on **a** PSNR, **b** SDME and **c** SSIM

It serves as a means of validating visual model, which is adjusted for contrast, structure, and brightness data so that SSIM is provided by,

$$\text{SSIM} = [\Omega(a_1, b_1)]^n [\Upsilon(a_1, b_1)]^T \left[\wp(a_1, b_1)\right]^K \tag{24}$$

Here, brightness is denoted as $\Omega(a_1, b_1)$, contrast is signified as $\Upsilon(a_1, b_1)$, the structure of the image is represented as $\wp(a_1, b_1)$, and n, T, K attribute is fixed to 1.

4.3 Experimental results

Figures 3 and 4 show the experimental outcomes of FJBA-NFS-IE-CGAN with a collection of input photos from the Hyperspectral Remote Sensing Scenes dataset and YOLO Object Detection dataset, respectively. Figures 3a and 4a show the collection of input images that were taken from the dataset. Figures 3b and 4b show the blurry image created using the blur pixel map finding technique. Figures 3c and 4c show display a reconstructed image.

4.4 Comparative methods

The techniques considered for the assessment include RDN [15], LSFNet [16], GRNN [2], Joint blur kernel estimation [17], GRNN + deep neural network (DNN) [35], deep generalized unfolding network (DGUNet) [36], PO-based NFS-IE-CGAN, HPO-based NFS-IE-CGAN, and proposed FJBA-NFS-IE-CGAN. By changing the levels of blur intensity, the assessment is done.

4.4.1 Analysis using hyperspectral remote sensing scenes dataset

(a) A*ssessment with the Indian Pines dataset*

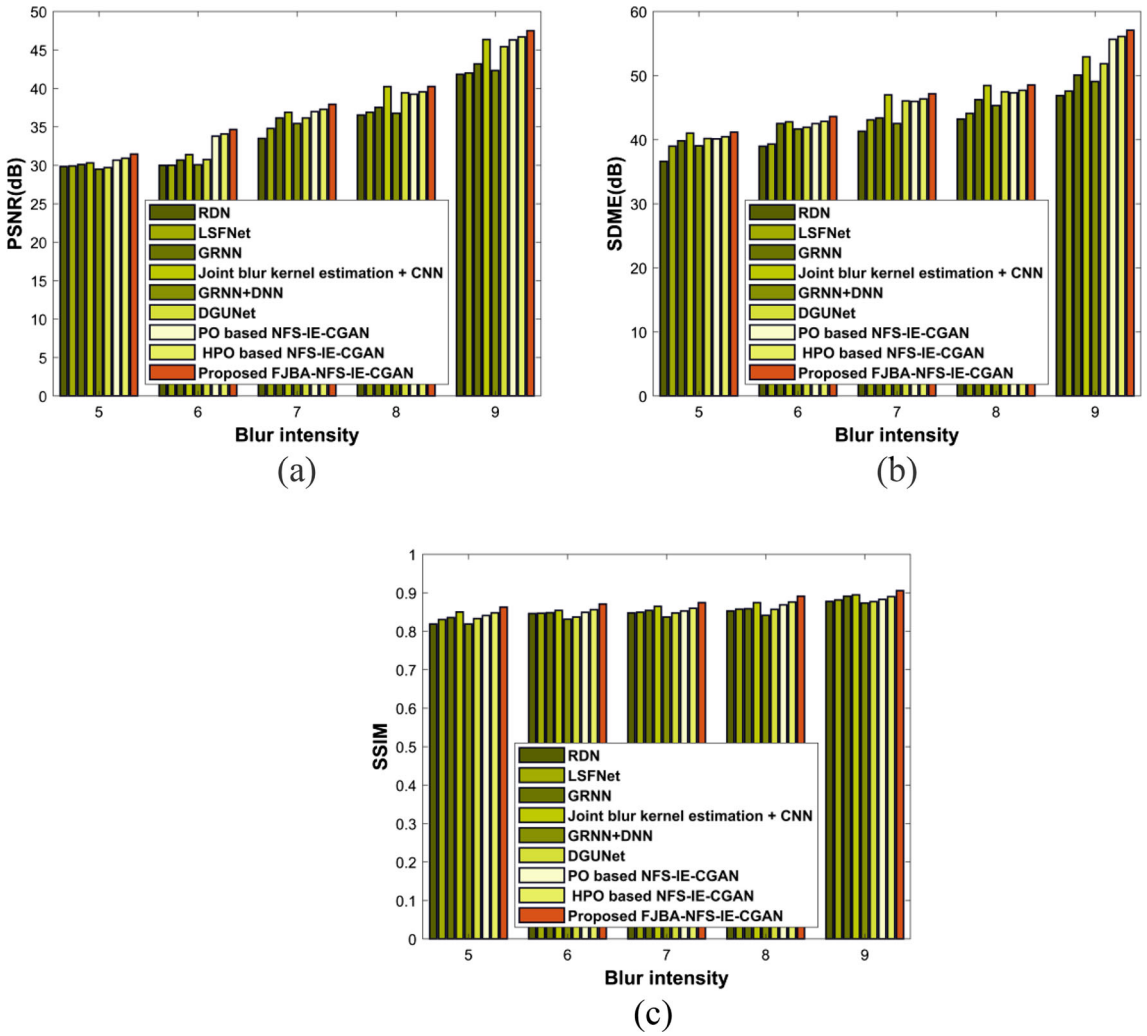

Fig. 7 Valuation with Pavia Centre and University dataset based on **a** PSNR, **b** SDME, and **c** SSIM

The evaluation with the Indian Pines dataset is revealed in Fig. 5. Figure 5a depicts the evaluation using PSNR. Moreover, PSNR measured by RDN, LSFNet, GRNN, joint blur kernel estimation, GRNN + CNN, DGUNet, PO-based NFS-IE-CGAN, HPO-based NFS-IE-CGAN, and suggested FJBA-NFS-IE-CGAN are 42.945, 44.699, 46.073, 48.341, 45.152, 47.374, 49.056, 49.458, and 50.314 dB when blur intensity is 9. The performance improvement of the proposed method is 14.64% higher than the existing method RDN. Figure 5b depicts the assessment using SDME. For a blur intensity of 9, the SDME as determined by RDN is 51.743 dB, LSFNet is 52.404 dB, GRNN is 53.078 dB, joint blur kernel estimation CNN is 54.874 dB, GRNN + CNN is 52.017 dB, DGUNet is 53.777 dB, PO-based NFS-IE-CGAN is 55.932 dB, HPO-based NFS-IE-CGAN is 56.391 dB, and proposed FJBA_NFS-IE-CGAN is 57.366 dB. The analysis of the FJBA-NFS-IE-CGAN with consideration for SSIM is shown in Fig. 5c. At a blur intensity of 9, the SSIM calculated by the FJBA_NFS-IE-CGAN is 0.963, which is greater by 0.927, 0.938, 0.953, 0.951, 0.934, 0.932, 0.939, and 0.947 than the SSIM assessed by methods like RDN, LSFNet, GRNN, joint blur kernel estimation, GRNN + CNN, DGUNet, PO-based NFS-IE-CGAN, and HPO-based NFS-IE-CGAN. The performance improvement of the proposed method is 2.59% higher than the existing method LSFNet.

(b) *Assessment with the Salinas dataset*

Figure 6 displays the assessment with the Salinas dataset. The valuation with PSNR is displayed in Fig. 6a. When the blur intensity is 9, PSNR is calculated using the following methods: RDN: 40.465 dB; LSFNet: 40.856 dB; GRNN: 43.039 dB; joint blur kernel estimation CNN: 47.221 dB; GRNN + CNN: 42.178 dB; DGUNet: 46.276 dB; PO-based NFS-IE-CGAN: 47.754 dB; and HPO-based NFS-IE-CGAN: 48.146 dB, whereas 48.979 dB is the value for the proposed FJBA-NFS-IE-CGAN. Figure 6b shows the

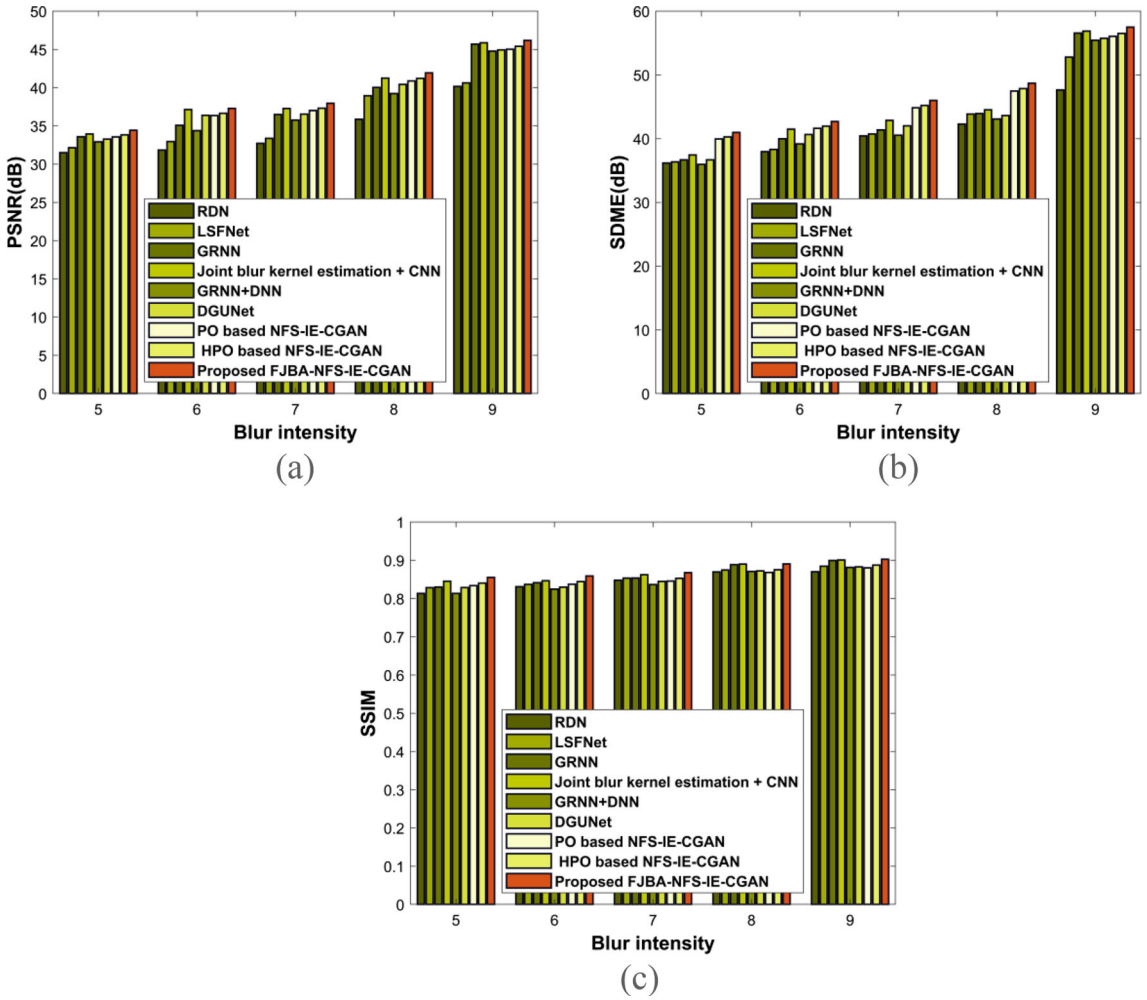

Fig. 8 Valuation with Cuprite datasets based on **a** PSNR, **b** SDME, and **c** SSIM

evaluation using SDME. Additionally, when the blur intensity is 9, the SDME measured by RDN, LSFNet, GRNN, joint blur kernel estimate, GRNN + CNN, DGUNet, PO-based NFS-IE-CGAN, and HPO-based NFS-IE-CGAN is 45.546, 47.711, 52.907, 54.818, 51.85, 53.72, 57.246, and 57.716 dB correspondingly, whereas the proposed FJBA-NFS-IE-CGAN is 58.714 dB. The performance improvement of the proposed method is 9.89% higher than the existing method GRNN. Figure 6c shows the results of the examination using SSIM. When blur intensity is 9, the suggested FJBA-NFS-IE-CGAN gained an SSIM of 0.970. Other methods, such as RDN, LSFNet, GRNN, joint blur kernel estimation, GRNN + CNN, DGUNet, PO-based NFS-IE-CGAN, and HPO-based NFS-IE-CGAN, achieved SSIM values of 0.922, 0.951, 0.952, 0.967, 0.933, 0.948, 0.946, and 0.953.

(c) *Assessment with Pavia Centre and University dataset*

Figure 7 displays the assessment with the Pavia Centre and University dataset. Figure 7a shows the evaluation with PSNR. When the blur intensity is 9, the PSNR calculated using RDN, LSFNet, GRNN, joint blur kernel estimation, GRNN + CNN, DGUNet, PO-based NFS-IE-CGAN, HPO-based NFS-IE-CGAN, and proposed FJBA-NFS-IE-CGAN is 44.502, 44.696, 45.944, 49.316, 45.03, 48.33, 49.272, 49.677, and 50.536 dB. The performance improvement of the proposed method is 2.50% higher than the existing method PO-based NFS-IE-CGAN. Figure 7b displays the results of the SDME assessment. In the case of a blur intensity of 9, the SDME as determined by RDN is 49.867 dB, LSFNet is 50.621 dB, GRNN is 53.279 dB, joint blur kernel estimation CNN is 56.301 dB, GRNN + CNN is 52.21 dB, DGUNet is 55.18 dB, PO-based NFS-IE-CGAN is 59.206 dB, HPO-based NFS-IE-CGAN is 59.691 dB, and suggested FJBA_NFS-IE-CGAN is 60.724 dB. The analysis of the FJBA_NFS-IE-CGAN with consideration for SSIM is shown in Fig. 7c. At a blur intensity of 9, the SSIM calculated by the FJBA_NFS-IE-CGAN is 0.963, which is more by 0.933, 0.938, 0.948, 0.952, 0.929, 0.933, 0.939, and 0.947 than the SSIM assessed by methods like RDN, LSFNet, GRNN, joint blur kernel estimation, GRNN + CNN,

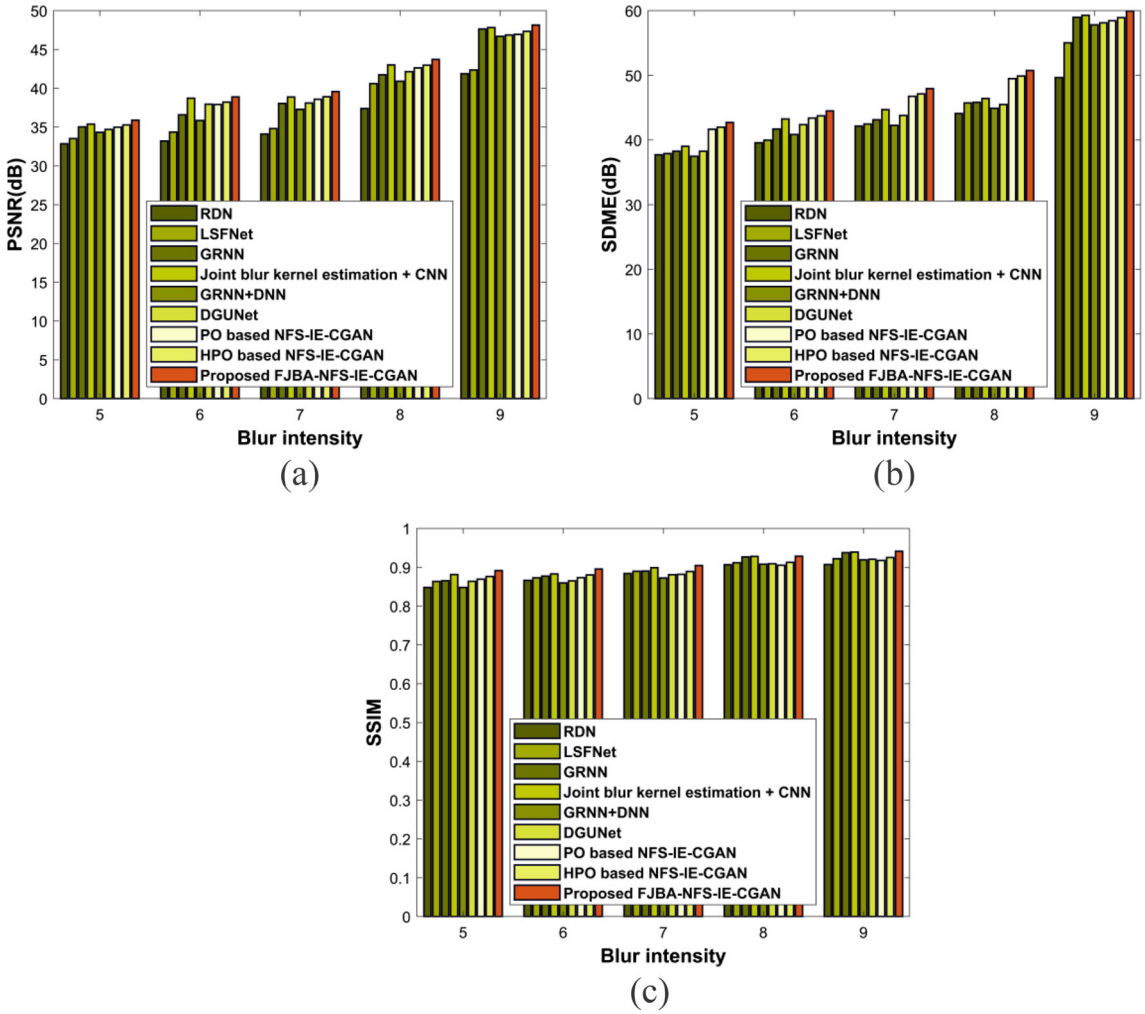

Fig. 9 Valuation with objection detection dataset based on **a** PSNR, **b** SDME, and **c** SSIM

DGUNet, PO-based NFS-IE-CGAN, and HPO-based NFS-IE-CGAN. The performance improvement of the proposed method is 1.66% higher than the existing method HPO-based NFS-IE-CGAN.

(d) *Assessment with Cuprite datasets*

Figure 8 shows an assessment with Cuprite datasets. Additionally, assessment with PSNR is shown in Fig. 8a. When blur intensity is 9, the PSNR evaluated by 42.724 dB for RDN, 43.216 dB for LSFNet, 48.612 dB for GRNN, 48.795 dB for joint blur kernel estimation_CNN, 47.640 dB for GRNN + CNN, 47.820 dB for DGUNet, 47.905 dB for PO-based NFS-IE-CGAN, and 48.298 dB for HPO-based NFS-IE-CGAN while that of proposed FJBA-NFS-IE-CGAN is 49.133 dB. The performance improvement of the proposed method is 13.04% higher than the existing method RDN. The assessment with SDME is presented in Fig. 8b. Also, when blur intensity is 9, SDME evaluated by RDN, LSFNet, GRNN, joint blur kernel estimation, GRNN + CNN, DGUNet, PO-based NFS-IE-CGAN, and HPO-based NFS-IE-CGAN are 50.674, 56.153, 60.187, 60.507, 58.983, 59.297, 59.633, and 60.123 dB, while that of proposed FJBA-NFS-IE-CGAN is 61.162 dB. The assessment with SSIM is presented in Fig. 8c. When blur intensity is 9, the proposed FJBA-NFS-IE-CGAN gained an SSIM of 0.960. The other techniques like RDN, LSFNet, GRNN, joint blur kernel estimation_CNN, GRNN + CNN, DGUNet, PO-based NFS-IE-CGAN, and HPO-based NFS-IE-CGAN attained SSIM of 0.926, 0.941, 0.957, 0.958, 0.938, 0.939, 0.936, and 0.944. The performance improvement of the proposed method is 1.97% higher than the existing method LSFNet.

4.4.2 Analysis using object detection dataset

Figure 9 shows an assessment with an Object detection dataset. The assessment with PSNR is shown in Fig. 9a. When blur intensity is 9, the PSNR evaluated by 41.870 dB

Table 1 Comparative discussion of proposed FJBA-NFS-IE-CGAN

Metrics	RDN	LSFNet	GRNN	Joint blur kernel estimation_CNN	GRNN + CNN	DGUNet	PO-based NFS-IE-CGAN	HPO-based NFS-IE-CGAN	Proposed FJBA_NFS-IE-CGAN
Indian Pines dataset									
PSNR (dB)	42.945	44.699	46.073	48.341	45.152	47.374	49.056	49.458	50.314
SSIM	0.927	0.938	0.953	0.951	0.934	0.932	0.939	0.947	0.963
SDME (dB)	51.743	52.404	53.078	54.874	52.017	53.777	55.932	56.391	57.366
Salinas dataset									
PSNR (dB)	40.465	40.856	43.039	47.221	42.178	46.276	47.754	48.146	48.979
SSIM	0.922	0.951	0.952	0.967	0.933	0.948	0.946	0.953	0.970
SDME (dB)	45.546	47.711	52.907	54.818	51.849	53.721	57.246	57.716	58.714
Pavia Centre and University dataset									
PSNR (dB)	44.502	44.696	45.944	49.316	45.025	48.330	49.272	49.677	**50.536**
SSIM	0.933	0.938	0.948	0.952	0.929	0.933	0.939	0.947	**0.963**
SDME (dB)	49.867	50.621	53.279	56.301	52.213	55.175	59.206	59.691	**60.724**
Cuprite dataset									
PSNR (dB)	42.724	43.216	48.612	48.795	47.640	47.820	47.905	48.298	49.133
SSIM	0.926	0.941	0.957	0.958	0.938	0.939	0.936	0.944	0.960
SDME (dB)	50.674	56.153	60.187	60.507	58.983	59.297	59.633	60.123	61.162
YOLO object detection dataset									
PSNR (dB)	41.870	42.352	47.640	47.820	46.687	46.863	46.947	47.332	48.151
SSIM	0.907	0.922	0.938	0.939	0.919	0.920	0.918	0.925	0.941
SDME (dB)	49.660	55.030	58.983	59.297	57.803	58.111	58.441	58.920	59.939

Table 2 Computational time

Methods	Computational time (seconds)
RDN	9.089
LSFNet	8.908
GRNN	7.090
Joint blur kernel estimation_CNN	6.987
GRNN + CNN	6.145
DGUNet	6.012
PO-based NFS-IE-CGAN	5.098
HPO-based NFS-IE-CGAN	5.003
Proposed FJBA_NFS-IE-CGAN	**4.982**

Bold value represents the best performance

for RDN, 42.352 dB for LSFNet, 47.640 dB for GRNN, 47.820 dB for joint blur kernel estimation_CNN, 46.687 dB for GRNN + CNN, 46.863 dB for DGUNet, 46.947 dB for PO-based NFS-IE-CGAN, and 47.332 dB for HPO-based NFS-IE-CGAN, while that of proposed FJBA-NFS-IE-CGAN is 48.151 dB. The assessment with SDME is presented in Fig. 9b. Also, when blur intensity is 9, SDME evaluated by RDN, LSFNet, GRNN, joint blur kernel estimation, GRNN + CNN, DGUNet, PO-based NFS-IE-CGAN, and HPO-based NFS-IE-CGAN are 49.660, 55.030, 58.983, 59.297, 57.803, 58.111, 58.441, and 58.920 dB, while that of proposed FJBA-NFS-IE-CGAN is 59.939 dB. The performance improvement of the proposed method is 1.59% higher than the Joint blur kernel estimation. The assessment with SSIM is presented in Fig. 9c. When blur intensity is 9, the proposed FJBA-NFS-IE-CGAN gained an SSIM of 0.941. The other techniques like RDN, LSFNet, GRNN, Joint blur kernel estimation_CNN, GRNN + CNN, DGUNet, PO-based NFS-IE-CGAN, and HPO-based NFS-IE-CGAN attained SSIM of 0.907, 0.922, 0.938, 0.939, 0.919, 0.920, 0.918, and 0.925.

4.5 Comparative discussion

The best results considering various datasets are displayed in Table 1. Here, the maximum PSNR, SSIM, and SDME of the proposed FJBA-NFS-IE-CGAN are 50.536 dB, 60.724 dB, and 0.963, respectively, for the blur intensity of 9.

4.6 Computational time

The computational time of the proposed and existing methods is shown in Table 2. From Table 2, it is noted that the proposed method has minimum computational time.

5 Conclusion

Along with image restoration, a novel optimization-driven classifier is constructed. The steps for identifying blurred images and improving them are depicted. For a variety of reasons, including low camera resolution, motion blur, noise, and other factors, images might deteriorate during the acquisition process. Even though image restoration techniques can remove haze from a degraded image, they are problematic for use in a real-time system since they necessitate numerous photographs from the same location. To solve this problem, the proposed FJBA enables image enhancement and blur pixel detection. Firstly, the blur pixel detection is done using the input blurry image provided in the dataset. The blur pixel identification is performed using a DRN trained with FJBA. FJBA is created by combining the JBA and the FC. Furthermore, the blurred image is deblurred using a fusion CNN approach tuned through PHO. PHO stands for PO and HPO. Lastly, the image is enhanced using the NFS and the IE-CGAN, which has been fine-tuned using FJBA. The proposed FJBA-NFS-IE-CGAN gives an enhanced performance with a maximum PSNR of 50.536 dB, SDME of 60.724 dB, and SSIM of 0.963 with a blur intensity of image-3. In future, another database is adapted to validate the feasibility of designed technique.

Acknowledgements I would like to express my very great appreciation to the co-authors of this manuscript for their valuable and constructive suggestions during the planning and development of this research work.

Author contribution All authors have made substantial contributions to conception and design, revising the manuscript, and the final approval of the version to be published. Also, all authors agreed to be accountable for all aspects of the work in ensuring that questions related to the accuracy or integrity of any part of the work are appropriately investigated and resolved.

Funding This research did not receive any specific funding.

Data availability Statlog (Landsat satellite) dataset "https://archive.ics.uci.edu/ml/datasets/Statlog+%28Landsat+Satellite%29" is assessed on March, 2023.

Declarations

Conflict of interest The authors declare no conflict of interest.

Ethical approval Not applicable.

Informed consent Not applicable.

References

1. Campisi, P., Egiazarian, K. (eds.): Blind image deconvolution: theory and applications. CRC Press, Boca Raton (2017)

2. Yang, H., Su, X., Chen, S., Zhu, W., Ju, C.: Efficient learning-based blur removal method based on sparse optimization for image restoration. PLoS ONE **15**(3), e0230619 (2020)
3. Trouvé, P., Champagnat, F., Le Besnerais, G., Idier, J.: Single image local blur identification. In: 2011 18th IEEE International Conference on Image Processing, pp. 613–616. IEEE (2011)
4. Jezierska, A., Talbot, H., Pesquet, J.C.: Spatially variant psf modeling in confocal macroscopy. In: 2018 IEEE 15th International Symposium on Biomedical Imaging (ISBI 2018), pp. 489–492. IEEE (2018)
5. Tezaur, R., Kamata, T., Hong, L., Slonaker, S.S.: A system for estimating optics blur psfs from test chart images. In: Digital Photography XI, vol. 9404, pp. 84–93. SPIE (2015)
6. Huang, Y., Chouzenoux, E., Elvira, V.: Probabilistic modeling and inference for sequential space-varying blur identification. IEEE Trans. Comput. Imaging **7**, 531–546 (2021)
7. Zamir, S.W., Arora, A., Khan, S., Hayat, M., Khan, F.S., Yang, M.H., Shao, L.: Learning enriched features for fast image restoration and enhancement. IEEE Trans. Pattern Anal. Mach. Intell. **45**(2), 1934–1948 (2022)
8. Maini, R., Aggarwal, H.: A comprehensive review of image enhancement techniques. arXiv preprint arXiv:1003.4053 (2010)
9. Agaian, S.S., Panetta, K., Grigoryan, A.M.: A new measure of image enhancement. In: IASTED International Conference on Signal Processing & Communication, pp. 19–22 (2000)
10. Singh, G., Mittal, A.: Various image enhancement techniques—a critical review. Int. J. Innov. Sci. Res. **10**(2), 267–274 (2014)
11. Sun, X., Zheng, L.: Dissecting person re-identification from the viewpoint of viewpoint. In: Proceedings of the IEEE/CVF Conference on Computer Vision and Pattern Recognition, pp. 608–617 (2019)
12. Pratt, S.G., Bell, J.L.: Analytical observational study of nonfatal motor vehicle collisions and incidents in a light-vehicle sales and service fleet. Accid. Anal. Prev. **129**, 126–135 (2019)
13. Shen, L., Yue, Z., Feng, F., Chen, Q., Liu, S., Ma, J.: Msr-net: Low-light image enhancement using deep convolutional network. arXiv preprint arXiv:1711.02488 (2017)
14. Li, G., Yang, Y., Qu, X., Cao, D., Li, K.: A deep learning based image enhancement approach for autonomous driving at night. Knowl. Based Syst. **213**, 106617 (2021)
15. Zhang, Y., Tian, Y., Kong, Y., Zhong, B., Fu, Y.: Residual dense network for image restoration. IEEE Trans. Pattern Anal. Mach. Intell. **43**(7), 2480–2495 (2020)
16. Chang, M., Feng, H., Xu, Z., Li, Q.: Low-light image restoration with short-and long-exposure raw pairs. IEEE Trans. Multimed. **24**, 702–714 (2021)
17. Huang, L., Xia, Y.: Joint blur kernel estimation and CNN for blind image restoration. Neurocomputing **396**, 324–345 (2020)
18. Wang, R.: Exploring Wavelet transform-based image enhancement algorithm for image restoration of long march national cultural park. J. Environ. Public Health (2022)
19. Panetta, K., KM, S.K., Rao, S.P., Agaian, S.S.: Deep perceptual image enhancement network for exposure restoration. IEEE Trans. Cybern. (2022)
20. Hyperspectral Remote Sensing Scenes dataset https://www.ehu.eus/ccwintco/index.php/Hyperspectral_Remote_Sensing_Scenes#Cuprite is assessed on June, 2023.
21. Kaur, A., Sharma, S., Mishra, A.: A novel Jaya-BAT algorithm-based power consumption minimization in cognitive radio network. Wirel. Pers. Commun. **108**, 2059–2075 (2019)
22. Zhao, C., Xue, D., Chen, Y.: A fractional order PID tuning algorithm for a class of fractional order plants. In: IEEE International Conference Mechatronics and Automation, vol. 1, pp. 216–221. IEEE (2005)
23. Trojovský, P., Dehghani, M.: Pelican optimization algorithm: a novel nature-inspired algorithm for engineering applications. Sensors **22**(3), 855 (2022)
24. Naruei, I., Keynia, F., Sabbagh Molahosseini, A.: Hunter–prey optimization: algorithm and applications. Soft. Comput. **26**(3), 1279–1314 (2022)
25. Vieira, J., Dias, F.M., Mota, A.: Neuro-fuzzy systems: a survey. In: 5th WSEAS NNA International Conference on Neural Networks and Applications, Udine, Italia, pp. 1–6 (2004)
26. Li, R., Pan, J., Li, Z., Tang, J.: Single image dehazing via conditional generative adversarial network. In: Proceedings of the IEEE Conference on Computer Vision and Pattern Recognition, pp. 8202–8211 (2018)
27. Chen, Z., Chen, Y., Wu, L., Cheng, S., Lin, P.: Deep residual network-based fault detection and diagnosis of photovoltaic arrays using current-voltage curves and ambient conditions. Energy Convers. Manag. **198**, 111793 (2019)
28. Bhaladhare, P.R., Jinwala, D.C.: A clustering approach for the-diversity model in privacy preserving data mining using fractional calculus-bacterial foraging optimization algorithm. Adv. Comput. Eng. (2014)
29. Rao, R.: Jaya: A simple and new optimization algorithm for solving constrained and unconstrained optimization problems. Int. J. Ind. Eng. Comput. **7**(1), 19–34 (2016)
30. Yang, X.S.: A new metaheuristic bat-inspired algorithm. In: Nature Inspired Cooperative Strategies for Optimization (NICSO 2010), pp. 65–74 (2010)
31. Ram Prabhakar, K., Sai Srikar, V., Venkatesh Babu, R.: Deepfuse: A deep unsupervised approach for exposure fusion with extreme exposure image pairs. In: Proceedings of the IEEE International Conference on Computer Vision, pp. 4714–4722 (2017)
32. Karaboga, D., Kaya, E.: Adaptive network based fuzzy inference system (ANFIS) training approaches: a comprehensive survey. Artif. Intell. Rev. **52**, 2263–2293 (2019)
33. Kuang, X., Sui, X., Liu, Y., Chen, Q., Gu, G.: Single infrared image enhancement using a deep convolutional neural network. Neurocomputing **332**, 119–128 (2019)
34. YOLO Object Detection dataset, https://www.kaggle.com/code/rahulkumarpatro/yolo-object-detection. Accessed June 2023
35. Kollem, S., Reddy, K.R., Sreejith, S., Prasad, C.R., Samala, S., Pardhu, T.: A general regression neural network based blurred image restoration. In: The Proceeding of Fourth International Conference on Emerging Research in Electronics, Computer Science and Technology (ICERECT). IEEE, Mandya, India (2022)
36. Mou, C., Wang, Q., Zhang, J.: Deep generalized unfolding networks for image restoration. In: The Proceeding of the IEEE/CVF Conference on Computer Vision and Pattern Recognition (CVPR), pp. 17399–17410 (2022)

Terms and Conditions

Springer Nature journal content, brought to you courtesy of Springer Nature Customer Service Center GmbH (“Springer Nature”).
Springer Nature supports a reasonable amount of sharing of research papers by authors, subscribers and authorised users (“Users”), for small-scale personal, non-commercial use provided that all copyright, trade and service marks and other proprietary notices are maintained. By accessing, sharing, receiving or otherwise using the Springer Nature journal content you agree to these terms of use (“Terms”). For these purposes, Springer Nature considers academic use (by researchers and students) to be non-commercial.
These Terms are supplementary and will apply in addition to any applicable website terms and conditions, a relevant site licence or a personal subscription. These Terms will prevail over any conflict or ambiguity with regards to the relevant terms, a site licence or a personal subscription (to the extent of the conflict or ambiguity only). For Creative Commons-licensed articles, the terms of the Creative Commons license used will apply.
We collect and use personal data to provide access to the Springer Nature journal content. We may also use these personal data internally within ResearchGate and Springer Nature and as agreed share it, in an anonymised way, for purposes of tracking, analysis and reporting. We will not otherwise disclose your personal data outside the ResearchGate or the Springer Nature group of companies unless we have your permission as detailed in the Privacy Policy.
While Users may use the Springer Nature journal content for small scale, personal non-commercial use, it is important to note that Users may not:

1. use such content for the purpose of providing other users with access on a regular or large scale basis or as a means to circumvent access control;
2. use such content where to do so would be considered a criminal or statutory offence in any jurisdiction, or gives rise to civil liability, or is otherwise unlawful;
3. falsely or misleadingly imply or suggest endorsement, approval , sponsorship, or association unless explicitly agreed to by Springer Nature in writing;
4. use bots or other automated methods to access the content or redirect messages
5. override any security feature or exclusionary protocol; or
6. share the content in order to create substitute for Springer Nature products or services or a systematic database of Springer Nature journal content.

In line with the restriction against commercial use, Springer Nature does not permit the creation of a product or service that creates revenue, royalties, rent or income from our content or its inclusion as part of a paid for service or for other commercial gain. Springer Nature journal content cannot be used for inter-library loans and librarians may not upload Springer Nature journal content on a large scale into their, or any other, institutional repository.
These terms of use are reviewed regularly and may be amended at any time. Springer Nature is not obligated to publish any information or content on this website and may remove it or features or functionality at our sole discretion, at any time with or without notice. Springer Nature may revoke this licence to you at any time and remove access to any copies of the Springer Nature journal content which have been saved.
To the fullest extent permitted by law, Springer Nature makes no warranties, representations or guarantees to Users, either express or implied with respect to the Springer nature journal content and all parties disclaim and waive any implied warranties or warranties imposed by law, including merchantability or fitness for any particular purpose.
Please note that these rights do not automatically extend to content, data or other material published by Springer Nature that may be licensed from third parties.
If you would like to use or distribute our Springer Nature journal content to a wider audience or on a regular basis or in any other manner not expressly permitted by these Terms, please contact Springer Nature at

onlineservice@springernature.com